Key Points:
- A 3-D model of upper crustal anisotropy in the vicinity of the SJFZ is proposed based on 1,694 pairs of splitting parameters at three stations
- Fast orientations are fault parallel for rays traversing the fault zones, and are parallel to regional stress for non-fault-crossing rays
- Apparent temporal variations of the splitting parameters after an M4.7 earthquake are mostly caused by changes in source distribution

Spatial Variations of Upper Crustal Anisotropy Along the San Jacinto Fault Zone in Southern California: Constraints From Shear Wave Splitting Analysis

Enyuan Jiang[1], Kelly H. Liu[1] , Yuan Gao[1,2] , Xiaofei Fu[3], and Stephen S. Gao[1]

[1]Geology and Geophysics Program, Missouri University of Science and Technology, Rolla, MO, USA, [2]Key Laboratory of Earthquake Prediction, Institute of Earthquake Forecasting, China Earthquake Administration, Beijing, China, [3]College of Earth Science and Research Institute of Unconventional Oil and Gas, Northeast Petroleum University, Daqing, Heilongjiang, China

Abstract   To discern spatial and explore possible existence of temporal variations of upper crustal anisotropy in an ~15 km section of the San Jacinto Fault Zone (SJFZ) that is composed of the Buck Ridge and Clark faults in southern California, we conduct a systematic shear wave splitting investigation using local S-wave data recorded by three broadband seismic stations located near the surface expression of the SJFZ. An automatic data selection and splitting measurement procedure is first applied, and the resulting splitting measurements are then manually screened to ensure reliability of the results. Strong spatial variations in crustal anisotropy are revealed by 1,694 pairs of splitting parameters (fast polarization orientation and splitting delay time), as reflected by the dependence of the resulting splitting parameters on the location and geometry of the raypaths. For raypaths traveling through the fault zones, the fast orientations are dominantly WNW-ESE which is parallel to the faults and may be attributed to fluid-filled fractures in the fault zones. For non-fault-zone crossing raypaths, the fast orientations are dominantly N–S which are consistent with the orientation of the regional maximum compressive stress. A three-dimensional model of upper crustal anisotropy is constructed based on the observations. An increase in the raypath length normalized splitting times is observed after the 03/11/2013 M4.7 earthquake, which is probably attributable to changes in the spatial distribution of earthquakes before and after the M4.7 earthquake rather than reflecting temporal changes of upper crustal anisotropy.

1. Introduction

When a shear wave propagates near vertically through a transversely isotropic medium with a horizontal axis of symmetry, it splits into two quasi-shear waves with orthogonal polarization orientations and different wave speeds (Ando, 1980). Shear wave splitting (SWS) is a direct manifestation of azimuthal anisotropy which can be quantified by the polarization orientation of the fast wave (fast orientation or φ) and the arrival time difference between the fast and slow waves (splitting time or δt). Laboratory and observational studies suggest that azimuthal anisotropy developed in the upper continental crust can generally be divided into two categories based on its formation mechanism. The first is stress-induced anisotropy from preferentially aligned fluid-filled microcracks that are mostly parallel to the maximum horizontal compressive stress direction (SHmax; Cao et al., 2019; Crampin & Booth, 1985; Crampin, 1987; Piccinini et al., 2006; Yang et al., 2011), and the second is structure-induced anisotropy that is mostly from fluid-filled fractures along fault zones (Cochran et al., 2020, 2003; Gao et al., 2019; Li et al., 2014; Zinke & Zoback, 2000), aligned terrane minerals (Okaya et al., 2016), and sedimentary layering (Audet, 2015). While it is a common practice in previous SWS studies to present station-averaged splitting parameters and interpret the measurements under the assumption that a single anisotropy-forming process dominates beneath a given station, some studies (e.g., Ando et al., 1980; Audoine et al., 2004; Graham et al., 2020; Zinke & Zoback, 2000) report individual measurements and explore spatial variations of the observed splitting parameters for the purpose of delineating the three-dimensional (3-D) distribution of anisotropic properties, a practice that is adopted in this study.

Owing to its high seismicity rate and structural complexity, the San Jacinto Fault Zone (SJFZ) of southern California, which is a constituent of the San Andreas fault system and is composed of the Buck Ridge Fault (BRF) and Clark Fault (CF) in the study area (Figure 1), is an ideal natural laboratory for applying the
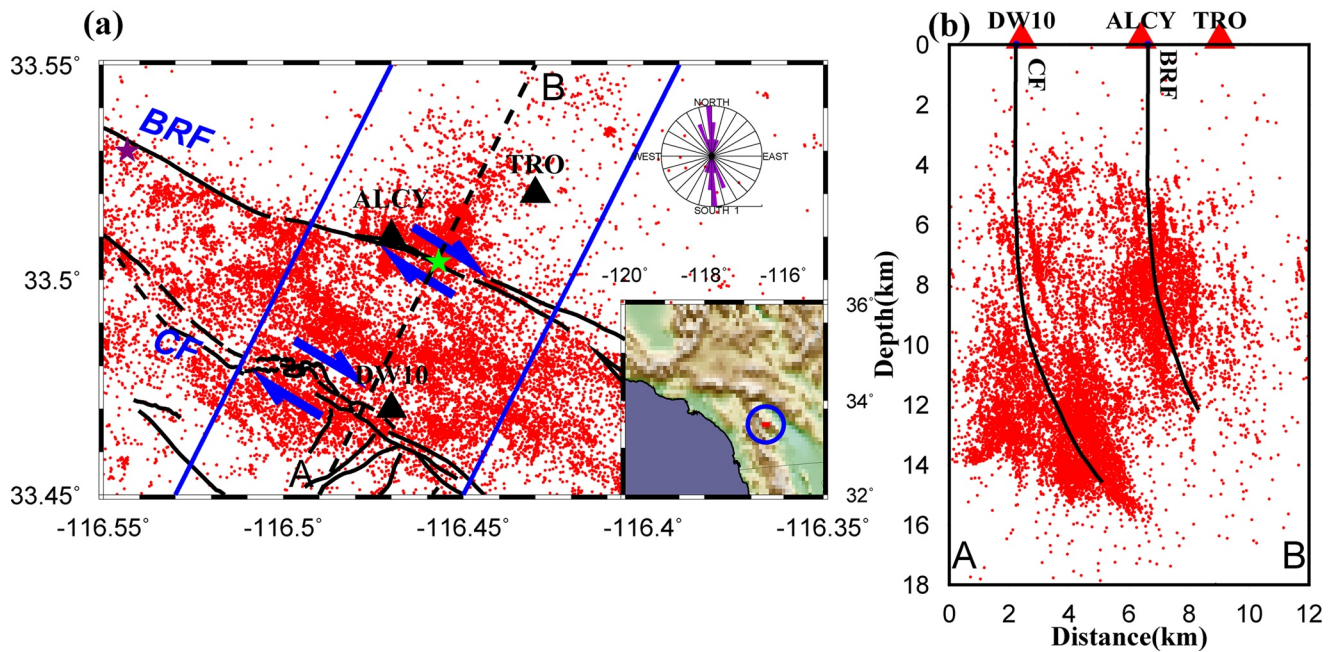
Figure 1. (a) Distribution of seismic stations (black triangles), major faults (black solid lines), and earthquakes that occurred from 1/1/1981 to 12/31/2017 (red dots) relocated by the Southern California Earthquake Data Center (https://scedc.caltech.edu/). The rose diagram shows the distribution of the orientation of the maximum horizontal compressive stress in the mapped area (Heidbach et al., 2018). The green star in the middle and the purple star in the upper left corner represent the epicenters of M4.7 and M5.2 earthquakes, respectively. The inset map of southern California shows the study area as a red rectangle inside the blue circle. (b) Cross section view for earthquakes (red dots) between the two blue lines in (a) projected to profile AB (dashed line in (a)). The fault planes (black lines) are based on Ross et al. (2017). BRF: Buck Ridge Fault. CF: Clark Fault.

SWS technique to investigate the spatial distribution and possible temporal variation of crustal anisotropy in the seismogenic zone associated with active strike slip faults (Mizuno et al., 2005). Both the BRF and CF are right-lateral strike-slip faults dipping toward the NNE (Figure 1b; Ross et al., 2017; Sharp, 1967), with a strike of about 115° (WNW-ESE) counted clockwise from the North and a GPS-determined slipping rate of 10–16 mm/year for the CF (Tymofyeyeva & Fialko, 2018) and 3.4–4 mm/year for the BRF (Onderdonk et al., 2015). The direction of SHmax determined by earthquake focal mechanisms is N–S (Heidbach et al., 2018). The main seismogenic zone for the CF has a depth range of 4–15 km, while that for the BRF is about 5–12 km (Figure 1b). In the study area, the two largest earthquakes over the past 20 years occurred on 06/12/2005 and 03/11/2013, with magnitudes of 5.2 and 4.7, respectively, both along the BRF (Figure 1a). By analyzing the seismicity distribution and focal mechanism solutions, Ross et al. (2017) observe a broad damage zone on the top 5 km of the BRF and CF. At the depth of 8–16 km, a complex active zone that consists of mixed strike-slip and normal fault in the area between the BRF and CF is also observed. They assume that the broad damage zone on the top 5 km is dominantly associated with the ongoing regional deformation, and the deeper structures are mainly caused by ductile deformation.

Li and Peng (2017) measure SWS parameters at more than 400 stations in southern California. At Station TRO which is the only station in our study area measured by Li and Peng (2017), a WNW-ESE station averaged fast orientation and a station averaged splitting time of 0.109 s are obtained. Li et al. (2015) report SWS parameters at four stations in the study area (Figure 1), including ALCY, DW10, TRO (which are used in the current study), and SROS (which is not used in the current study due to a limited number of reliable observations). The station averaged fast orientations are N–S, N–S, and WNW-ESE, and the splitting times are 0.103 s, 0.079 s, and 0.078 s for stations ALCY, DW10, and TRO, respectively. They attribute the N–S fast orientations to SHmax, and the WNW-ESE fast orientations to fault-parallel fractures. Boness and Zoback (2006) measure SWS at 86 stations in California with no stations in our study area, and report mostly N–S fast orientations in the general area and propose that the N–S oriented SHmax is mostly responsible for the observed upper crustal anisotropy in the off-fault regions. Results from previous investigations in the study area are mostly presented as station-averaged splitting parameters under the assumption that the
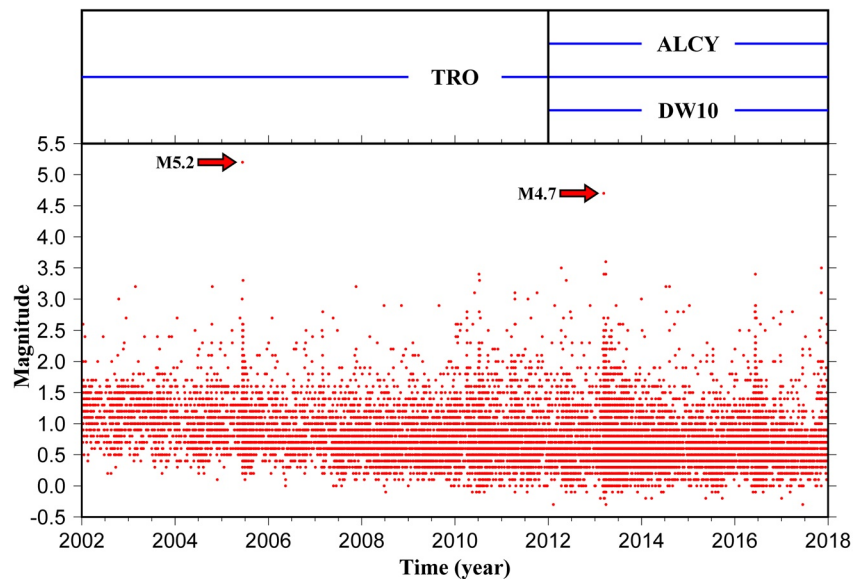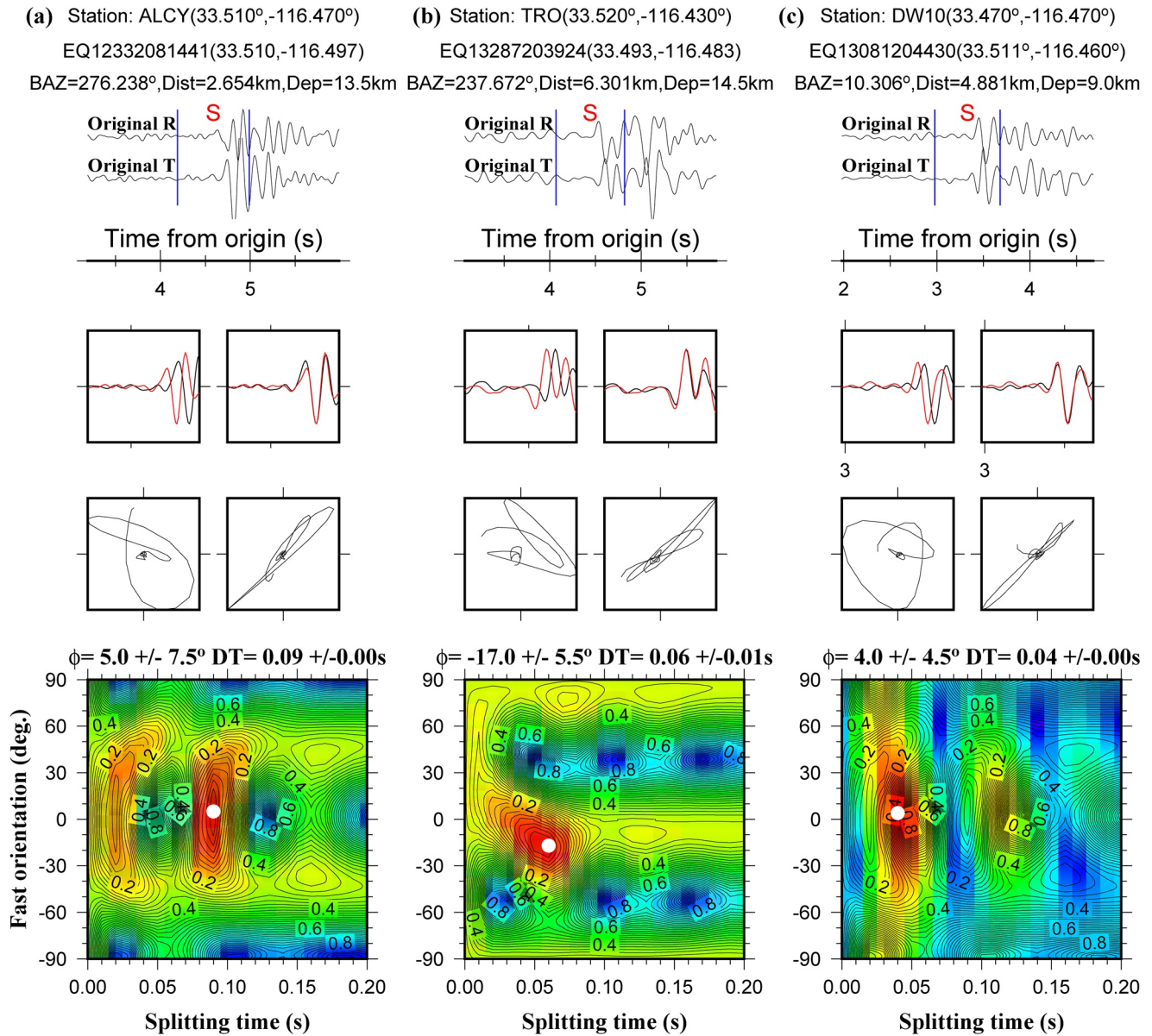
Figure 2. Magnitude −0.3 and greater earthquakes that occurred in the study area. The recording period of each of the three stations is shown at the top of the plot.

source of anisotropy is directly beneath the stations. As demonstrated below and by numerous previous studies conducted elsewhere (e.g., Graham et al., 2020; Zinke & Zoback, 2000), considering the geometry of the raypath can provide critical additional information regarding the anisotropy structure and crustal stress field for the study area.

In addition to spatial variations of the splitting parameters, temporal variations have been observed in some previous SWS studies. Such variations have been mostly attributed to temporal variations in anisotropy-forming processes, including increased magma pressure which can affect the stress orientations (Miller & Savage, 2001; Volti & Crampin, 2003), localized stress changes (Gao & Crampin, 2003, 2004; Hiramatsu et al., 2010), and stress and rock physical property changes associated with earthquakes (e.g., Cao et al., 2019; Crampin et al., 1990; Gao et al., 1998; Kaviris et al., 2017; Lucente et al., 2010). However, spatial variations of the splitting parameters could be erroneously interpreted as temporal variations owing to changes in the location of the seismic sources (Liu et al., 2008b; Peng & Ben-Zion, 2005). In this study we take the advantage of the recent availability of a relocated earthquake catalog produced by the Southern California Data Center and the high quality waveform data to explore the 3-D spatial and possible temporal variations of upper crustal anisotropy in the vicinity of the CF and BRF branches of the SJFZ in southern California.

2. Data and Methods

The seismic data used in this study were recorded by three stations (ALCY, TRO, and DW10) over the period of 2002–2017 (Figures 1 and 2) and were obtained from the Incorporated Research Institutions for Seismology (IRIS) Data Management Center. The relocated earthquake catalog was obtained from the Southern California Earthquake Data Center (https://scedc.caltech.edu/), which contains 22,622 magnitude ≥−0.3 earthquakes in the mapped area of Figure 1a for the period of 1/1/1981–12/31/2017. For the shear wave splitting analysis, a total of 11,184 magnitude ≥−0.3 earthquakes occurred during 2002–2017 were used. Station DW10 is situated inside the CF zone and provided data from 2012 to 2017; ALCY is located at the surface expression of the BRF and the recording period is nearly the same as DW10; and TRO is about 2 km northeast of the BRF, and recorded waveform data from 2002 to 2017 (Figures 1a and 2). To minimize the distortion of the free surface on the direct S-wave waveforms, only events in the S-wave window, which is dependent on the velocity structure beneath the study area, but can be approximately defined by a maximum incident angle of about 35° (Booth & Crampin, 1985), were used in the study.

(a) Station: ALCY(33.510º,-116.470º)

EQ12332081441(33.510,-116.497)

BAZ=276.238º,Dist=2.654km,Dep=13.5km

(b) Station: TRO(33.520º,-116.430º)

EQ13287203924(33.493,-116.483)

BAZ=237.672º,Dist=6.301km,Dep=14.5km

(c) Station: DW10(33.470º,-116.470º)

EQ13081204430(33.511º,-116.460º)

BAZ=10.306º,Dist=4.881km,Dep=9.0km

Figure 3. Examples of splitting analysis from three seismic stations (a, b, and c). For each column, from the top to the bottom: original and transverse components, unshifted and shifted fast and slow components, particle motion patterns, and corrected transverse energy contour map. The solid white circle represents the optimal pairs of splitting parameters which correspond to the minimum energy on the corrected component with an orientation that is orthogonal to the pre-splitting polarization direction of the shear wave. DT: splitting time.

The original seismograms were bandpass filtered using corner frequencies of 0.5 and 10 Hz. An automatic data selection procedure was then applied to reject events with an S-wave signal-to-noise ratio (SNR) less than 3.0 on the filtered radial component. The procedure for measuring shear wave splitpleating parameters is described in details in Liu and Gao (2013) and is based on the criterion of minimizing the lesser of the two eigenvalues of the covariance matrix of the seismograms after the correction for anisotropy (Silver & Chan, 1991). The optimal pair of splitting parameters corresponds to the maximum linearity in the corrected fast and slow components. In addition to the optimal pair of splitting parameters, the procedure also searches for the optimal azimuth along which the pre-splitting shear wave is polarized (Silver & Chan, 1991). To provide a visual display for evaluating the uniqueness of the optimal pair of splitting parameters, the procedure corrects the horizontal components based on both the optimal pair of splitting

parameters and the optimal azimuth to produce a contour map of the remaining energy on the corrected "transverse" component (see plots in the bottom row of Figure 3). Note that the "transverse" orientation referred here is the orientation that is orthogonal to the optimal azimuth of pre-splitting polarization which is usually different from the orientation of the great circle arc. For ensuring the quality and reliability of the automatically obtained results, all the splitting measurements were manually screened to adjust the limits of the time window used for splitting analysis to only include robust direct S-wave arrivals. Additionally, the ranking determined by the automatic process (Liu et al., 2008a) was adjusted for some of the measurements based on the quality of the signal, linearity of the corrected particle motion pattern, as well as the strength and uniqueness of the minimum energy value point on the contour map of the corrected transverse component (Figure 3).

3. Results

A total of 1,694 pairs of well-defined splitting parameters, including 530 for ALCY, 926 for DW10, and 238 for TRO were obtained (Table S1). To illustrate the 3-D distribution of crustal anisotropy, in Figure 4, we plot the splitting parameters at the stations (which is the most commonly used approach in previous studies), the mid-points between the stations and epicenters, and at the epicenters. Additionally, results from each of the stations are displayed separately in Figure 5, where the splitting times are normalized by the length of the raypath.

The fast orientations observed at the two fault zone stations, ALCY and DW10, are dominantly N–S, while those at the off-fault station (TRO) are mostly WNW-ESE (Figure 4). The average splitting times are 0.12 ± 0.04, 0.05 ± 0.03, and 0.05 ± 0.03 s for stations ALCY, DW10, and TRO, respectively, and the corresponding raypath length normalized splitting times (NSTs) are 13.55 ± 6.91, 4.77 ± 2.48, and 3.98 ± 2.40 ms/km, respectively. Note that the value after the plus/minus sign represents one standard deviation of the sample.

3.1. ALCY

The majority of the events recorded by Station ALCY on and to the SW of the BRF possess N–S fast orientations, and those to the NE of the BRF demonstrate fault-parallel fast orientations (Figure 5d). The latter group of events have larger NST values than those in the former group, with the largest NST values directly beneath the station (Figure 5f). The splitting times observed at ALCY are the greatest among all the three stations (Figure 5e). The circular mean of the 530 fast orientation measurements is $-15.64 \pm 24.45°$, and the mean splitting time is 0.12 ± 0.04 s. Li et al. (2015) report a station dominant fast orientation of 2.5° and a mean splitting time of 0.103 ± 0.061 s, which are comparable with our results.

3.2. DW10

Station DW10 has the most SWS measurements (926) which are dominated by N–S fast orientations (Figure 5g), with a circular mean of $-4.14 \pm 32.58°$ and a mean splitting time of 0.05 ± 0.03 s. The fast orientations observed from events to the NE of the CF are mostly N–S, while the prevailing fast orientations of events to the SW of the CF are fault-parallel (Figure 5g). No obvious spatial variations of the NST values are observed at this station (Figure 5i). For this station, Li et al. (2015) obtained a station dominant fast orientation of 17° and a mean splitting time of 0.079 ± 0.068 s.

3.3. TRO

The fast orientations observed at Station TRO are dominantly fault-parallel (Figure 5a) with a circular mean of $-45.09 \pm 23.90°$, which is comparable to the station dominant result of $-67°$ reported in Li et al. (2015). The splitting times range from 0.01 to 0.13 s with an average value of 0.05 ± 0.03 s, and the NSTs range from 0.64 to 14.69 ms/km with an average value of 3.98 ± 2.40 ms/km. Both the total splitting times and the NSTs from events located to the NE of the BRF are larger than those observed from events to the SW side of the fault (Figures 5b and 5c).
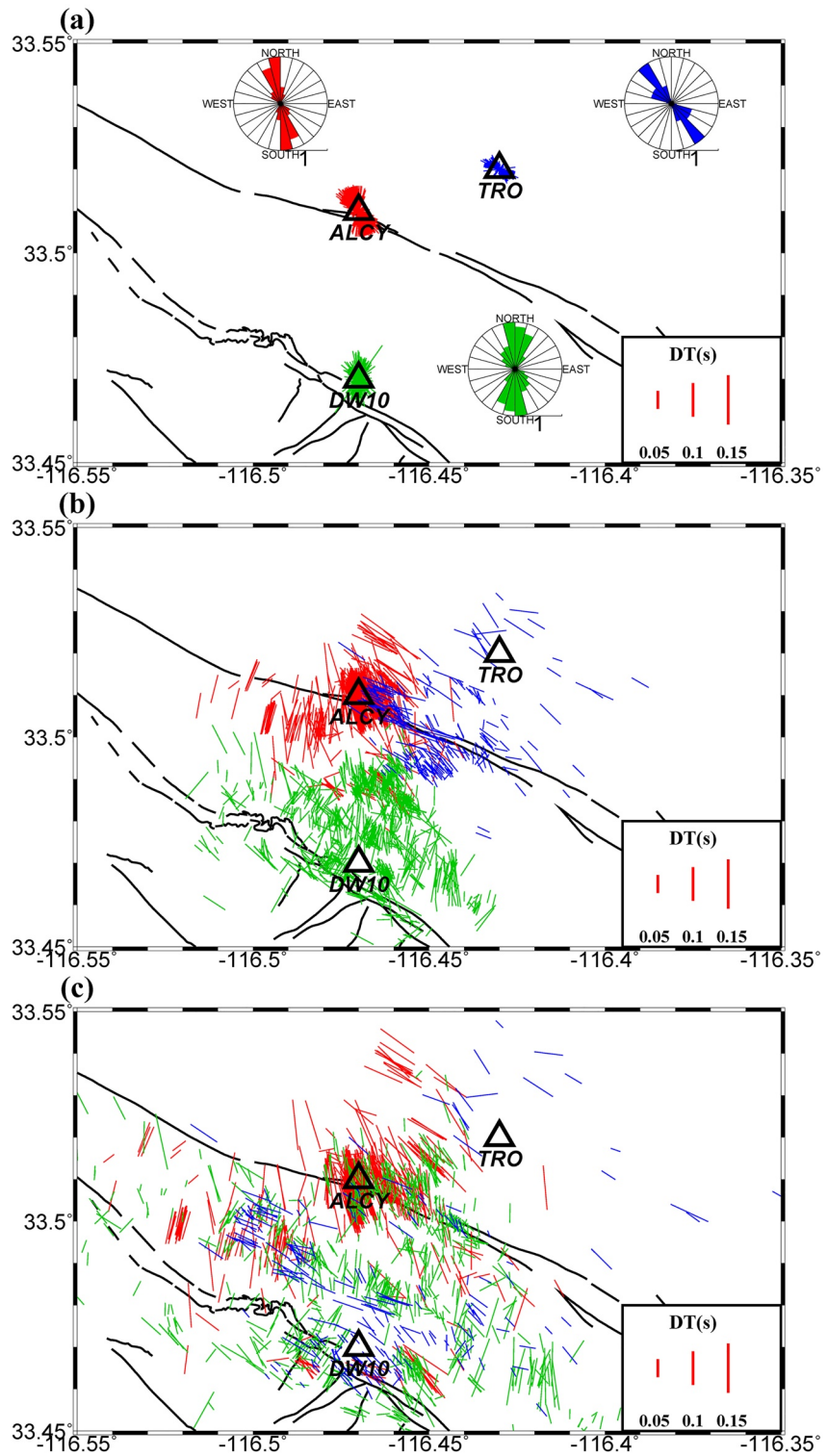
Figure 4. Results of shear wave splitting analysis for stations TRO (blue symbols), ALCY (red), and DW10 (green) plotted at (a) the stations, (b) the middle points between the epicenters and stations, and (c) the epicenters. The orientation of bars reflects the fast orientation, and the length of the bars is proportional to the splitting time. The stations are represented by the open triangles.
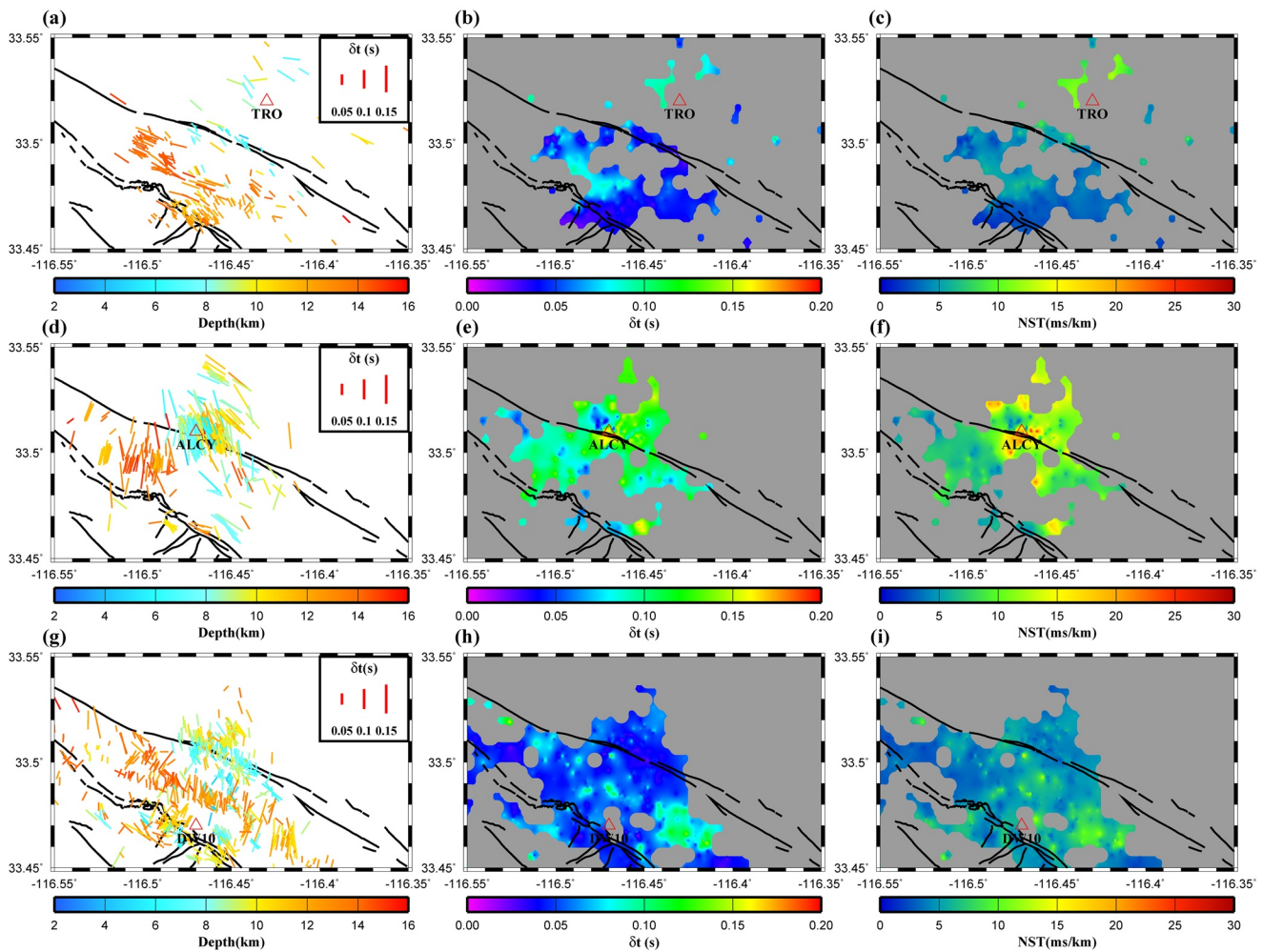
Figure 5. Resulting splitting parameters for stations TRO (a, b, and c), ALCY (d, e, and f), and DW10 (g, h, and i) plotted at the epicenters. The left panel shows the fast orientations and splitting times, with the color of bars representing the focal depth. The middle and right columns show the total splitting times and raypath length normalized splitting times, respectively, which were produced by spatially smoothing the measurements and masking the areas without data. The stations are represented by the red triangles.

4. Discussion

4.1. Three-Dimensional Variations of Upper Crustal Anisotropy

Most previous SWS studies in the study area use station averaged (or station dominant) local S-waves splitting parameters to investigate the spatial distributions of anisotropy characteristics, a practice that is incapable of revealing possible raypath dependent splitting parameters associated with the 3-D heterogeneity of crustal anisotropy. Additionally, in areas with strong anisotropy heterogeneities like the study area, the individual splitting parameters observed at a given station may vary as a function of the azimuth and focal depth of the events (Figure 5), as observed by numerous previous studies (e.g., Graham et al., 2020; Zinke & Zoback, 2000). Consequently, the station averaged splitting parameters may be biased toward measurements in the most populous event clusters, possibly resulting in misleading implications of the actual anisotropy structure. In this study, on the basis of previously determined fault geometry (Ross et al., 2017) and by taking the advantage of the large number of high quality measurements, we build a 3-D anisotropy model (Figure 6) that fits the majority of the splitting measurements. Major characteristics of the model include: (1) in the vicinity of the two fault zones, the observed shear wave splitting is dominated by structurally induced anisotropy with a fault-parallel fast orientation; (2) anisotropy in areas outside the fault zones is stress induced with a nearly N–S fast orientation that is parallel to SHmax (Zhang & Schwartz, 1994); (3)
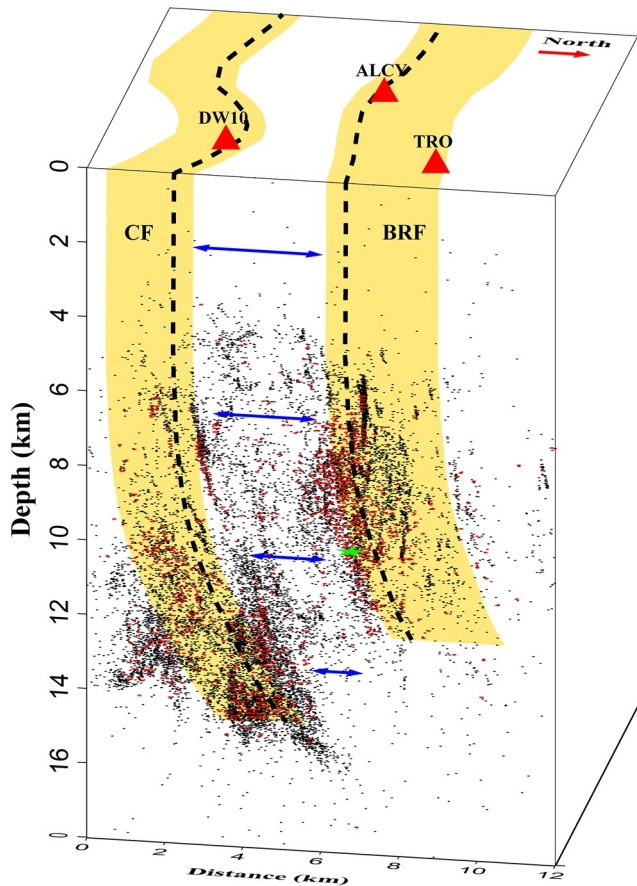
Figure 6. A schematic model showing the three-dimensional distribution of anisotropic properties. Areas shaded in orange are dominated by fault-parallel (WNW-ESE) fast orientations. Anisotropy in the rest of the area has a N–S (SHmax parallel) fast orientation and a strength that decreases with depth (indicated by the orientation and length of the double-headed arrows, respectively). Black dots are events shown in Figure 1b, red dots are events used for shear wave splitting analysis, and the green star is the location of the M4.7 earthquake projected to Profile AB in Figure 1a.

the anisotropy strength for both structurally and stress induced anisotropy decreases with depth due to increasing lithostatic pressure (Lin & Schmandt, 2014; Nur & Simmons, 1969; Parisi et al., 2018). In the following we attempt to validate the model by comparing the predicted and observed splitting parameters for each of the stations, under the approximation that the two types of anisotropy are nearly orthogonal to each other in the study area. For a raypath traveling through two regions of anisotropy with non-parallel and non-orthogonal fast orientations, the observed splitting parameters vary as a function of the back azimuth of the raypaths, with a 90° periodicity (Silver & Savage, 1994). When the two fast orientations are 90° apart from each other, the resulting splitting time is the difference between the individual splitting times of the two layers, and the fast orientation is the same as that of the layer with the larger splitting time (Pastori et al., 2019; Silver & Savage, 1994). If the two fast orientations are close but are not exactly orthogonal to each other, such as the scenario for the study area where the stress-induced fast orientation is nearly N–S and the fault zones have an average orientation of about 115° clockwise from the North, the aforementioned relationships between the observed splitting parameters and those of the individual layers still hold for most of the back-azimuths. Note that the 115° fault strike was calculated using the coordinates of the two ends of the BRF in the area mapped in Figure 1, and local variations of the strike can be observed. In particular, some segments of the faults, such as the portion near Station ALCY of the BRF and the portion near Station DW10 of the CF, are more E–W oriented than the rest of the faults.

4.1.1. Station ALCY

Events that occurred in the area to the SW of the BRF mainly display SHmax parallel N–S fast orientations, which can be explained by the fact that a large portion of the raypath do not travel through the fault zones (Figure 7b) but through the SHmax controlled anisotropic region between the BRF and CF. In contrast, raypaths from events located to the NE of the BRF are mostly in the fault zone, leading to the observed fault-parallel fast orientations. Relative to the other two stations, the shear waves recorded by ALCY only travel through one type of medium, which, when combined with the anticipated greater degree of anisotropy near the BRF, may explain the large splitting times (Figures 5e and 5f).

4.1.2. Station DW10

For events that occurred between the BRF and CF, the raypaths arrived at Station DW10 mostly traveled through the medium affected by SHmax, leading to the observed N–S fast orientations (Figures 5g and 7c). On the other hand, raypaths from events located to the SW of the CF are mostly in the fault zone and therefore the splitting measurements from these events are dominated by fault parallel fast orientations.

4.1.3. Station TRO

The raypaths of the events located to the NE of the surface expression of the NNE-dipping BRF mainly travel through the structurally induced anisotropic medium controlled by the strike slip fault, resulting in the observed dominantly fault parallel fast orientations (Figures 5 and 7a). Raypaths from events located to the SW of the BRF travel through a deep layer dominated by stress induced anisotropy with a low anisotropy strength and arrive at the station after traveling through a shallow layer possessing structurally induced anisotropy with a stronger anisotropy strength. Because the fast orientations of the stress induced and structurally induced anisotropies are approximately orthogonal to each other and the latter has a greater strength, the fast orientations are dominantly fault parallel, as observed. The partial cancellation of the
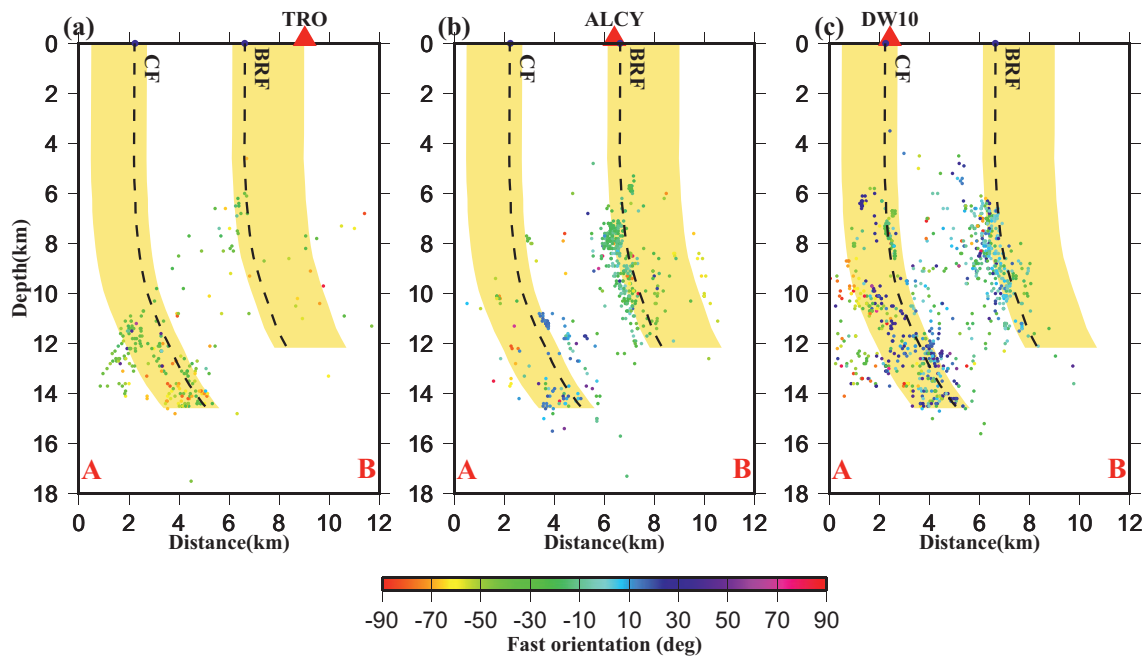
Figure 7. Cross-section views of the schematic model shown in Figure 6 for stations (a) TRO, (b) ALCY, and (c) DW10. Dots are events with SWS measurements, and the colors of the dots indicate the fast orientations.

splitting times can also explain the greater splitting times observed in the area NE of the BRF relative to the SW side (Figures 5b and 5c).

4.2. Apparent Temporal Variations of Splitting Parameters

We next explore possible temporal variations of the splitting parameters, which, if present, could indicate changes in the orientation and strength of crustal stress related to an array of important tectonic processes such as magma movement and earthquake preparation (e.g., Cao et al., 2019; Gao & Crampin, 2003, 2004; Miller & Savage, 2001; Volti & Crampin, 2003). Figure 8 shows the apparent temporal variations of the NSTs and the fast orientations observed at the three stations for a 6-year period starting from 2012. Among the possible changes, the most significant one is the NST values observed at ALCY before and after the 03/11/2013 M4.7 earthquake, from ~5 ms/km before the earthquake to ~20 ms/km afterward (Figure 8c). An increase in the NST values with a smaller magnitude is also observed at Station TRO (Figure 8a). Over the several years following the M4.7 Earthquake, the NST values for both stations decreased gradually and eventually reached the pre-earthquake level. Such a variation, if it is real, could imply the development and healing of fractures associated with the M4.7 earthquake.

To assess whether the apparent temporal variations of the splitting parameters are caused by temporal changes of the locations of the earthquakes (Liu et al., 2008b; Peng & Ben-Zion, 2005), in Figure 9 we plot the splitting parameters in a 1-year time window before and after the M4.7 earthquake. Before the earthquake, the splitting measurements obtained at Station ALCY are mostly from events located to the SW of the BRF (Figure 9c). The focal depths of the events are mostly greater than 10 km. Immediately after the earthquake, the splitting measurements obtained at this station are mostly from shallower events (which are dominantly aftershocks of the M4.7 main shock) located on or to the NE of the BRF (Figure 9d). Because the total splitting times for the two groups of events are approximately the same (Figure 5e), the shallower events following the M4.7 main shock resulted in larger NSTs. Therefore, the apparent large increase in the NSTs after the M4.7 earthquake observed at ALCY (Figure 8c) is mostly caused by the change of earthquake locations and focal depths. For Station TRO, although such a feature is not as obvious due to the fewer number of measurements (Figures 9a and 9b), it is clear that the observed apparent NST variation at this station is also the result of spatial changes of event locations after the M4.7 earthquake. Some events with
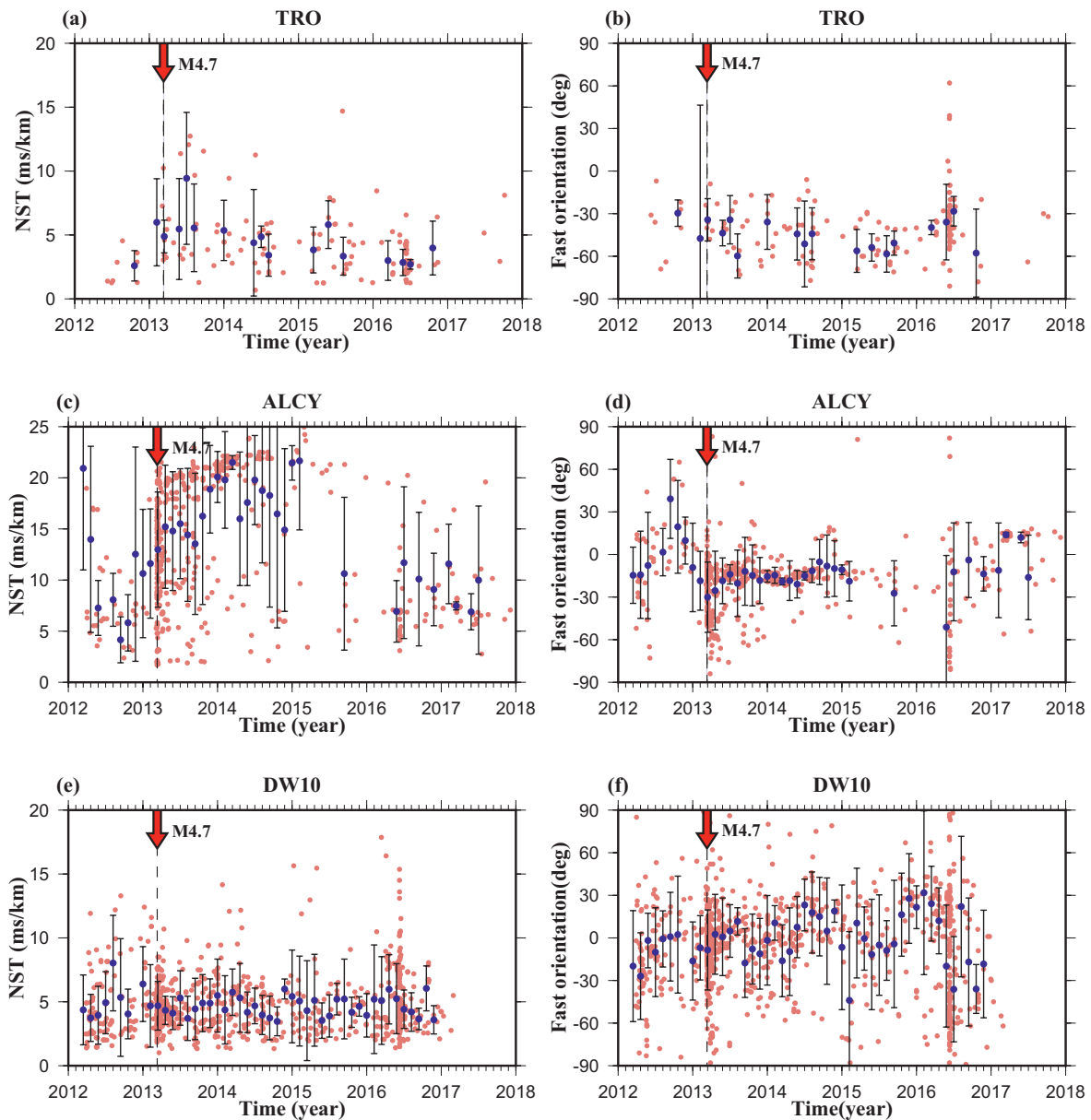
Figure 8. Temporal variations of the observed NSTs (left column) and fast orientations (right column) for Station (a) and (b) TRO, (c) and (d) ALCY, and (e) and (f) DW10. The red dots are individual measurements, and the blue dots with error bars are averaged measurements in 0.1-year windows. The red arrow indicates the M4.7 earthquake. NSTs, normalized splitting times.

large NSTs occurred in the area to the NE of the BRF in the 1-year window after the M4.7 earthquake (Figure 9b), while almost all the measurements for the pre-earthquake 1-year window were located to the SW of the fault (Figure 9a).

5. Conclusions

Systematic spatial variations of upper crustal anisotropy are observed by utilizing 1,694 pairs of splitting parameters using shear waves from local earthquakes recorded by three stations situated in the vicinity of the BRF and CF. The vast majority of the fast orientations are either WNW-ESE which is parallel to the strike of the faults, or N–S which aligns with the orientation of the maximum horizontal compressive stress. The observed spatial variations of the fast orientations and the splitting times can be satisfactorily explained by
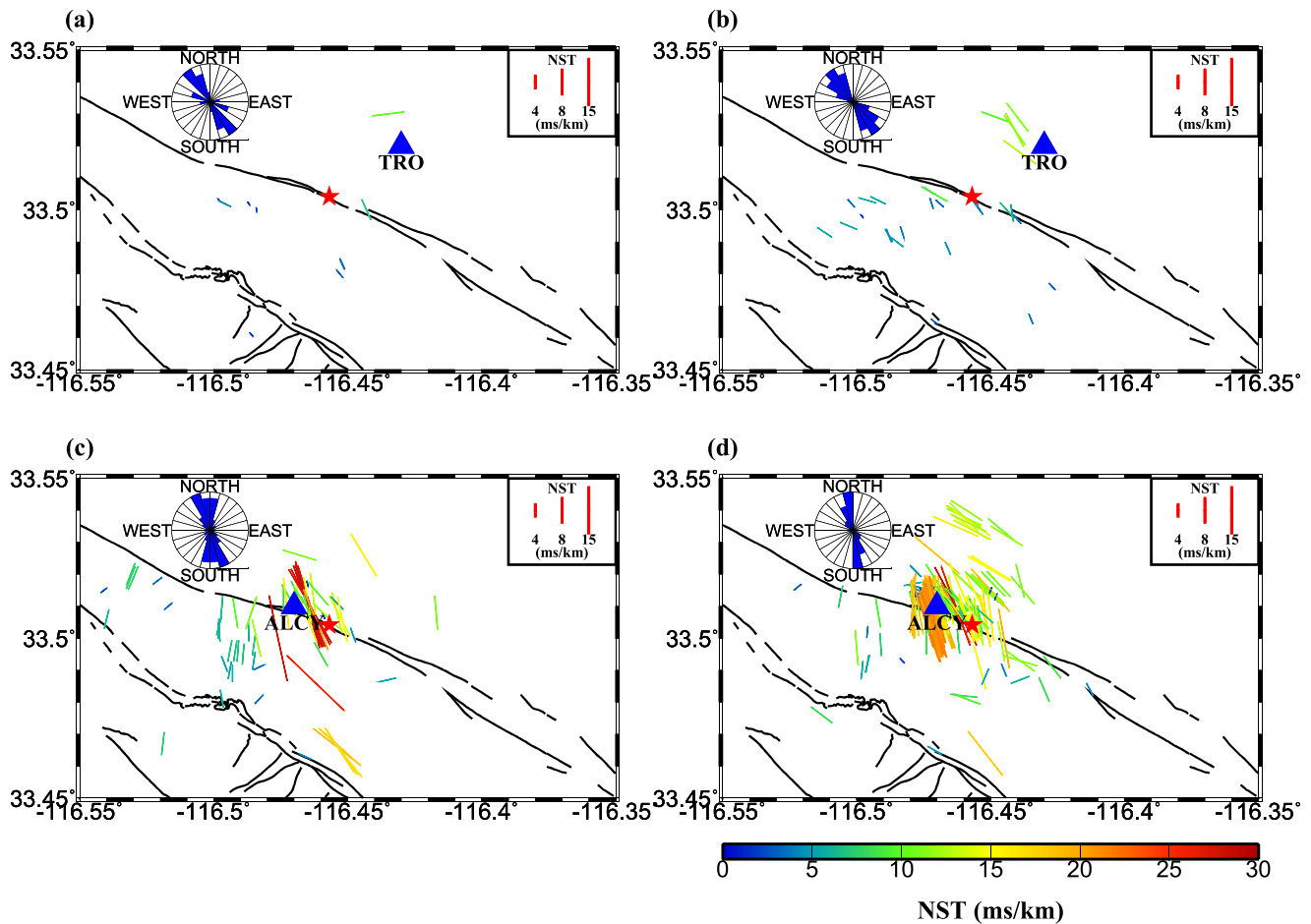
Figure 9. Splitting parameters observed one year before (left panels) and one year after (right panels) the 3/11/2013 M4.7 earthquake at stations (a) and (b) TRO, and (c) and (d) ALCY. Colors indicate the NSTs. The red stars represent the epicenter of the M4.7 earthquake, and the rose diagrams show the fast orientations from events in the 1-year period. NSTs, normalized splitting times.

a 3-D model which is composed of a zone of fracture-controlled anisotropy adjacent to the faults, and areas of regional stress affected anisotropy away from the fault zones. The strength of both types of anisotropy decreases with depth. Temporal variations of the splitting parameters are observed at two of the stations, which are mostly caused by temporal variations of the earthquake foci rather than reflecting temporal changes of anisotropy characteristics. The study demonstrates the feasibility of using a large number of splitting measurements to delineate spatial and possible temporal variations in crustal anisotropy and associated geodynamic processes.

Data Availability Statement

All the data used in this study are publicly available from the IRIS Data Management Center (https://ds.iris.edu/ds/nodes/dmc; Last accessed: January 2019), and the catalog of the relocated hypocenters was obtained from the Southern California Earthquake Data Center (https://scedc.caltech.edu/).

References

Ando, M., Ishikawa, Y., & Wada, H. (1980). S-wave anisotropy in the upper mantle under a volcanic area in Japan. *Nature*, *286*(5768), 43–46. https://doi.org/10.1038/286043a0

Audet, P. (2015). Layered crustal anisotropy around the San Andreas fault near Parkfield, California. *Journal of Geophysical Research: Solid Earth*, *120*(5), 3527–3543. https://doi.org/10.1002/2014JB011821

Audoine, E., Savage, M. K., & Gledhill, K. (2004). Anisotropic structure under a back arc spreading region, the Taupo Volcanic Zone, New Zealand. *Journal of Geophysical Research*, *109*(B11). https://doi.org/10.1029/2003JB002932

Boness, N. L., & Zoback, M. D. (2006). Mapping stress and structurally controlled crustal shear velocity anisotropy in California. *Geology*, *34*(10), 825–828. https://doi.org/10.1130/G22309.1

Booth, D. C., & Crampin, S. (1985). Shear-wave polarizations on a curved wavefront at an isotropic free surface. *Geophysical Journal International*, *83*(1), 31–45. https://doi.org/10.1111/j.1365-246X.1985.tb05154.x

Cao, L., Kao, H., Wang, K., Chen, C., Mori, J., Ohmi, S., & Gao, Y. (2019). Spatiotemporal variation of crustal anisotropy in the Source Area of the 2004 Niigata, Japan Earthquake. *Bulletin of the Seismological Society of America*, *109*(4), 1331–1342. https://doi.org/10.1785/0120180195

Cochran, E. S., Skoumal, R. J., McPhillips, D., Ross, Z. E., & Keranen, K. M. (2020). Activation of optimally and unfavorably oriented faults in a uniform local stress field during the 2011 Prague, Oklahoma, sequence. *Geophysical Journal International*, *222*(1), 153–168. https://doi.org/10.1093/gji/ggaa153

Cochran, E. S., Vidale, J. E., & Li, Y. G. (2003). Near-fault anisotropy following the Hector Mine earthquake. *Journal of Geophysical Research*, *108*(B9). https://doi.org/10.1029/2002JB002352

Crampin, S. (1987). Geological and industrial implications of extensive-dilatancy anisotropy. *Nature*, *328*(6130), 491. https://doi.org/10.1038/328491a0

Crampin, S., & Booth, D. C. (1985). Shear-wave polarizations near the North Anatolian Fault – II. Interpretation in terms of crack-induced anisotropy. *Geophysical Journal International*, *83*(1), 75–92. https://doi.org/10.1111/j.1365-246X.1985.tb05157.x

Crampin, S., Booth, D. C., Evans, R., Peacock, S., & Fletcher, J. B. (1990). Changes in shear wave splitting at Anza near the time of the North Palm Springs Earthquake. *Journal of Geophysical Research*, *95*(B7), 11197–11212. https://doi.org/10.1029/JB095iB07p11197

Gao, Y., Chen, A., Shi, Y., Zhang, Z., & Liu, L. (2019). Preliminary analysis of crustal shear-wave splitting in Sanjiang lateral collision zone of the SE margin of the Tibetan Plateau and its tectonic implications. *Geophysical Prospecting*, *67*, 2432–2449. https://doi.org/10.1111/1365-2478.12870

Gao, Y., & Crampin, S. (2003). Temporal varitions of shear-wave splitting in field and laboratory studies in China. *Journal of Applied Geophysics*, *54*(3–4), 279–287. https://doi.org/10.1016/j.jappgeo.2003.01.002

Gao, Y., & Crampin, S. (2004). Observations of stress relaxation before earthquakes. *Geophysical Journal International*, *157*(2), 578–582. https://doi.org/10.1111/j.1365-246X.2004.02207.x

Gao, Y., Wang, P., Zheng, S., Wang, M., Chen, Y., & Zhou, H. (1998). Temporal changes in shear-wave splitting at an isolated swarm of small earthquakes in 1992 near Dongfang, Hainan Island, southern China. *Geophysical Journal International*, *135*(1), 102–112. https://doi.org/10.1046/j.1365-246X.1998.00606.x

Graham, K. M., Savage, M. K., Arnold, R., Zal, H. J., Okada, T., Iio, Y., & Matsumoto, S. (2020). Spatio-temporal analysis of seismic anisotropy associated with the Cook Strait and Kaikoura earthquake sequences in New Zealand. *Geophysical Journal International*, *223*, 1987–2008. https://doi.org/10.1093/gji/ggaa433

Heidbach, O., Rajabi, M., Cui, X., Fuchs, K., Müller, B., Reinecker, J., et al. (2018). The World Stress Map database release 2016: Crustal stress pattern across scales. *Tectonophysics*, *744*, 484–498. https://doi.org/10.1016/j.tecto.2018.07.007

Hiramatsu, Y., Iwatsuki, K., Ueyama, S., & Iidaka, T. (2010). Spatial variation in shear wave splitting of the upper crust in the zone of inland high strain rate, central Japan. *Earth Planets and Space*, *62*(9), 675–684. https://doi.org/10.5047/eps.2010.08.003

Kaviris, G., Spingos, I., Kapetanidis, V., Papadimitriou, P., Voulgaris, N., & Makropoulos, K. (2017). Upper crust seismic anisotropy study and temporal variations of shear-wave splitting parameters in the Western Gulf of Corinth (Greece) during 2013. *Physics of the Earth and Planetary Interiors*, *269*, 148–164. https://doi.org/10.1016/j.pepi.2017.06.006

Li, Z., & Peng, Z. (2017). Stress-and structure-induced anisotropy in southern California from two decades of shear wave splitting measurements. *Geophysical Research Letters*, *44*(19), 9607–9614. https://doi.org/10.1002/2017GL075163

Li, Z., Peng, Z., Ben-Zion, Y., & Vernon, F. L. (2015). Spatial variations of shear wave anisotropy near the San Jacinto Fault Zone in Southern California. *Journal of Geophysical Research: Solid Earth*, *120*(12), 8334–8347. https://doi.org/10.1002/2015JB012483

Li, Z., Zhang, H., & Peng, Z. (2014). Structure-controlled seismic anisotropy along the Karadere–Düzce branch of the North Anatolian Fault revealed by shear-wave splitting tomography. *Earth and Planetary Science Letters*, *391*, 319–326. https://doi.org/10.1016/j.epsl.2014.01.046

Lin, F. C., & Schmandt, B. (2014). Upper crustal azimuthal anisotropy across the contiguous US determined by Rayleigh wave ellipticity. *Geophysical Research Letters*, *41*(23), 8301–8307. https://doi.org/10.1002/2014GL062362

Liu, K. H., & Gao, S. S. (2013). Making reliable shear-wave splitting measurements. *Bulletin of the Seismological Society of America*, *103*(5), 2680–2693. https://doi.org/10.1785/0120120355

Liu, K. H., Gao, S. S., Gao, Y., & Wu, J. (2008a). Shear wave splitting and mantle flow associated with the deflected Pacific slab beneath northeast Asia. *Journal of Geophysical Research*, *113*(B1). https://doi.org/10.1029/2007JB005178

Liu, Y., Zhang, H., Thurber, C., & Roecker, S. (2008b). Shear wave anisotropy in the crust around the San Andreas fault near Parkfield: Spatial and temporal analysis. *Geophysical Journal International*, *172*(3), 957–970. https://doi.org/10.1111/j.1365-246X.2007.03618.x

Lucente, F. P., De Gori, P., Margheriti, L., Piccinini, D., Di Bona, M., Chiarabba, C., & Agostinetti, N. P. (2010). Temporal variation of seismic velocity and anisotropy before the 2009 MW 6.3 L'Aquila earthquake, Italy. *Geology*, *38*(11), 1015–1018. https://doi.org/10.1130/G31463.1

Miller, V., & Savage, M. (2001). Changes in seismic anisotropy after volcanic eruptions: Evidence from Mount Ruapehu. *Science*, *293*(5538), 2231–2233. https://doi.org/10.1126/science.1063463

Mizuno, T., Ito, H., Kuwahara, Y., Imanishi, K., & Takeda, T. (2005). Spatial variation of shear-wave splitting across an active fault and its implication for stress accumulation mechanism of inland earthquakes: The Atotsugawa fault case. *Geophysical Research Letters*, *32*(20). https://doi.org/10.1029/2005GL023875

Nur, A., & Simmons, G. (1969). Stress-induced velocity anisotropy in rock: An experimental study. *Journal of Geophysical Research*, *74*, 6667–6674. https://doi.org/10.1029/JB074i027p06667

Okaya, D., Christensen, N. I., Ross, Z. E., & Wu, F. T. (2016). Terrane-controlled crustal shear wave splitting in Taiwan. *Geophysical Research Letters*, *43*(2), 556–563. https://doi.org/10.1002/2015GL066446

Onderdonk, N. W., McGill, S. F., & Rockwell, T. K. (2015). Short-term variations in slip rate and size of prehistoric earthquakes during the past 2000 years on the northern San Jacinto fault zone, a major plate-boundary structure in southern California. *Lithosphere*, *7*, 211–234. https://doi.org/10.1130/L393.1

Parisi, L., Ferreira, A. M., & Ritsema, J. (2018). Apparent splitting of S waves propagating through an isotropic lowermost mantle. *Journal of Geophysical Research: Solid Earth*, *123*(5), 3909–3922. https://doi.org/10.1002/2017JB014394

Pastori, M., Baccheschi, P., & Margheriti, L. (2019). Shear wave splitting evidence and relations with stress field and major faults from the "Amatrice-Visso-Norcia Seismic Sequence". *Tectonics*, *38*(9), 3351–3372. https://doi.org/10.1029/2018TC005478

Peng, Z., & Ben-Zion, Y. (2005). Spatiotemporal variations of crustal anisotropy from similar events in aftershocks of the 1999 M 7.4 Izmit and M 7.1 Düzce, Turkey, earthquake sequences. *Geophysical Journal International*, *160*(3), 1027–1043. https://doi.org/10.1111/j.1365-246X.2005.02569.x

Piccinini, D., Margheriti, L., Chiaraluce, L., & Cocco, M. (2006). Space and time variations of crustal anisotropy during the 1997 Umbria—Marche, central Italy, seismic sequence. *Geophysical Journal International*, *167*(3), 1482–1490. https://doi.org/10.1111/j.1365-246X.2006.03112.x

Ross, Z. E., Hauksson, E., & Ben-Zion, Y. (2017). Abundant off-fault seismicity and orthogonal structures in the San Jacinto fault zone. *Science advances*, *3*(3). e1601946. https://doi.org/10.1126/sciadv.1601946

Sharp, R. V. (1967). San Jacinto fault zone in the Peninsular Ranges of southern California. *Geological Society of America Bulletin*, *78*(6), 705–730. https://doi.org/10.1130/0016-7606(1967)78[705:SJFZIT]2.0.CO;2

Silver, P. G., & Chan, W. W. (1991). Shear wave splitting and subcontinental mantle deformation. *Journal of Geophysical Research*, *96*(B10), 16429–16454. https://doi.org/10.1029/91JB00899

Silver, P. G., & Savage, M. K. (1994). The interpretation of shear-wave splitting parameters in the presence of two anisotropic layers. *Geophysical Journal International*, *119*(3), 949–963. https://doi.org/10.1111/j.1365-246X.1994.tb04027.x

Tymofyeyeva, E., & Fialko, Y. (2018). Geodetic evidence for a blind fault segment at the southern end of the San Jacinto fault zone. *Journal of Geophysical Research: Solid Earth*, *123*(1), 878–891. https://doi.org/10.1002/2017JB014477

Volti, T., & Crampin, S. (2003). A four-year study of shear-wave splitting in Iceland: 2. Temporal changes before earthquakes and volcanic eruptions. *Geological Society, London, Special Publications*, *212*(1), 135–149. https://doi.org/10.1144/GSL.SP.2003.212.01.09

Yang, Z., Sheehan, A., & Shearer, P. (2011). Stress-induced upper crustal anisotropy in southern California. *Journal of Geophysical Research*, *116*(B2). https://doi.org/10.1029/2010JB007655

Zhang, Z., & Schwartz, S. Y. (1994). Seismic anisotropy in the shallow crust of the Loma Prieta segment of the San Andreas fault system. *Journal of Geophysical Research*, *99*(B5), 9651–9661. https://doi.org/10.1029/94JB00241

Zinke, J. C., & Zoback, M. D. (2000). Structure-related and stress-induced shear-wave velocity anisotropy: Observations from microearthquakes near the Calaveras Fault in Central California. *Bulletin of the Seismological Society of America*, *90*(5), 1305–1312. https://doi.org/10.1785/01199